



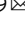


Evidence of pseudogravitational distortions of the Fermi surface geometry in the antiferromagnetic metal FeRh

Joseph Sklenar^{1,2,3}, Soho Shim ^{2,3}, Hilal Saglam^{4,5}, Junseok Oh^{2,3}, M. G. Vergniory^{6,7}, Axel Hoffmann ^{2,3,4,8,9}, Barry Bradlyn ^{2,10}, Nadya Mason^{2,3} & Matthew J. Gilbert ⁹ 

The confluence between high-energy physics and condensed matter has produced groundbreaking results via unexpected connections between the two traditionally disparate areas. In this work, we elucidate additional connectivity between high-energy and condensed matter physics by examining the interplay between spin-orbit interactions and local symmetry-breaking magnetic order in the magnetotransport of thin-film magnetic semimetal FeRh. We show that the change in sign of the normalized longitudinal magnetoresistance observed as a function of increasing in-plane magnetic field results from changes in the Fermi surface morphology. We demonstrate that the geometric distortions in the Fermi surface morphology are more clearly understood via the presence of pseudogravitational fields in the low-energy theory. The pseudogravitational connection provides additional insights into the origins of a ubiquitous phenomenon observed in many common magnetic materials and points to an alternative methodology for understanding phenomena in locally-ordered materials with strong spin-orbit interactions.

¹Department of Physics and Astronomy, Wayne State University, Detroit, MI 48201, USA. ²Department of Physics, University of Illinois at Urbana-Champaign, Urbana, IL 61801, USA. ³Materials Research Laboratory, University of Illinois at Urbana-Champaign, Urbana, IL 61801, USA. ⁴Materials Science Division, Argonne National Laboratory, Lemont, IL 60439, USA. ⁵Department of Physics, Yale University, New Haven, CT 06520, USA. ⁶Donostia International Physics Center, P. Manuel de Lardizabal 4, 20018 Donostia-San Sebastian, Spain. ⁷Max Planck Institute for Chemical Physics of Solids, Dresden D-01187, Germany. ⁸Department of Materials Science and Engineering, University of Illinois at Urbana-Champaign, Urbana, IL 61801, USA. ⁹Department of Electrical and Computer Engineering, University of Illinois at Urbana-Champaign, Urbana, IL 61801, USA. ¹⁰Institute for Condensed Matter Theory, University of Illinois at Urbana-Champaign, Urbana, IL 61801, USA. ✉email: matthewg@illinois.edu

The principles of symmetry and symmetry breaking form one of the cornerstones of our understanding of physics. The advent of topological materials has reinforced this fact, while also highlighting the points where symmetry principles alone cannot provide sufficient understanding of a diverse array of materials such as insulators^{1,2}, superconductors³, semimetals^{4–6} and magnets^{7,8}. Of the multitude of materials that have been shown to harbor topological phases, the interplay between band topology and local order in topological superconductors and topological magnets are of particular interest as it is unclear as to the manner in which symmetry and topology compete to control the observable properties of the underlying material. Magnetic metals possess many beneficial aspects compared to superconductors, that may lead to device applicability, such as high Curie temperatures. The high-temperature magnetic phase permits the observation of the competition between topology and magnetism to be explored at temperatures in excess of room temperature in topological magnets. Within this context, the interplay between topology and magnetic order^{9–11} allows for deeper insights into hitherto under-explored experimental signatures observed in both emergent and well-known materials.

In this work, we provide evidence that the interaction between the local magnetic order and spin-orbit coupling manifest in field-tunable distortions of the Fermi surface geometry in FeRh thin films. We use magnetotransport measurements in conjunction with detailed *ab-initio* and theoretical analysis to show that the thin-film form of antiferromagnetically-ordered (AFM) metal FeRh is a Weyl metal. Furthermore, we demonstrate that the anisotropic magnetoresistance (AMR), measured as a function of the field angle and current direction, may be understood in terms of changes in the Fermi surface topology brought about by geometric distortions that take the form of a coupling of electrons at the Fermi surface to pseudogravitational fields. In this work, we define “pseudogravitational” to refer to geometric distortions of the Fermi surface brought about by the interplay between the electronic bands and the applied electromagnetic fields that mimic the effects of gravity without possessing the properties inherent in true gravitational fields. We demonstrate through simple models that the theoretical mapping of the distorted Fermi surface to a pseudogravitational metric allows for a coherent and consistent understanding of magnetotransport in clean spin-orbit coupled metals, both with and without nontrivial topology. One of the crucial limitations in probing topological magnetic metals is their lack of tunability: typical knobs such as strain, external magnetic field, and chemical substitution are limited in their ability to change topological properties. We argue that one potential remedy to this problem is to exploit the interplay between spin-orbit coupling and local symmetry breaking order. The onset of magnetic order, for instance, is known to drastically alter band structure, allowing for the realization of additional symmetries that have resulted in the observation of topological phases harbored in previously unexplored metals and insulators^{7–11}.

Results and discussion

Magnetic and electronic structure of antiferromagnetic FeRh.

The FeRh films we examine are sputter-deposited onto a [001]-oriented MgO substrate¹². Epitaxial growth occurs such that the [100]-direction of the FeRh grows along the [110]-direction of the MgO, as illustrated in Fig. 1a. Although bulk FeRh is cubic, biaxial strain from the lattice mismatch with the substrate causes a small lattice distortion, such that the lattice constant of FeRh along the [001]-direction is ~2% larger than the in-plane lattice constant¹³. Furthermore, first-principles calculations suggest that in the antiferromagnetic phase the crystal is additionally

orthorhombically distorted in the plane of the MgO¹⁴. Complete details on the film growth and structural characterization are found in the Methods, and Supplementary Note 1 of the Supplementary Materials (SM) respectively.

In bulk FeRh, a metamagnetic phase transition between a ferromagnetic phase at high-temperatures and an antiferromagnetic phase at low-temperatures exists near room temperature¹⁵. Thinner films tend to have a depressed transition temperature¹⁶. At low magnetic fields, or fields much less than the exchange energy, our 20 nm thin films have a metamagnetic transition temperature of ~290 K. Experimental verification of the transition may be found in Supplementary Note 1. To understand the nature of the thin-film FeRh metamagnetic transition, we examine the band structure under the application of an in-plane magnetic field using density functional theory (DFT). At zero field in the AFM phase, the magnetic moments on the Fe atoms are taken to be collinear, and there is no magnetic moment on the Rh atoms. By applying an external field, a canted non-collinear AFM spin structure is induced and the Rh atoms develop a ferromagnetic moment in the direction of the applied field, as illustrated Fig. 1a. In Fig. 1b, we show the resultant DFT calculations of the electronic band structure of thin-film FeRh corresponding to the collinear (top) and non-collinear (bottom) spin structures. The collinear magnetic structure has the symmetries of magnetic space group P_4/m , where we have accounted for the orthorhombic distortion of the thin film form of FeRh¹⁴. Examining the DFT results, we observe several large electron pockets at the Fermi level throughout the Brillouin zone. The non-collinear magnetic structure shown in Fig. 1b corresponds to a magnetic field that is oriented along the [100]-direction, as indicated in Fig. 1a. Within the DFT calculations, the applied in-plane magnetic field is modeled through a non-zero ferromagnetic Rh moment that points in the same direction as the applied magnetic field. In the presence of the non-zero Rh moment, we observe significant Fermi surface reconstruction, leading to the emergence of topological nodes close to the Fermi level. The non-collinear structure has no orientation-reversing symmetries, and so allows for topologically charged Weyl fermions at generic points in the Brillouin zone; the Weyl fermions seen in Fig. 1b are pinned to high-symmetry lines in the Brillouin zone by twofold rotational symmetry. We utilize the observations obtained via the DFT calculations of thin-film FeRh to precondition the 8-band tight-binding model parameters that are discussed in Sec. III A 1 and is explored in more detail in Supplementary Note 3 of the SM.

For magnetotransport measurements, the films are patterned into Hall bars using a photolithographic and ion-milling process. In all transport measurements, the relative angle between the in-plane magnetic field and the applied current is denoted by ϕ . Representative field-dependent magnetoresistance effects in the AFM phase of FeRh are shown for $\phi = 0^\circ$ and 90° in Fig. 1c. A ferromagnetic contribution to the magnetoresistance in Fig. 1c is evident as a small peak when the field is swept at $\phi = 90^\circ$. The peak arises from ferromagnetic AMR of the FeRh near the MgO interface as the magnetization rotates from being parallel to perpendicular to the current¹⁷. Hysteresis in the magnetoresistance disappears near 1 T, and is consistent with magnetometry data that shows the residual ferromagnetic moment saturating at a field magnitude below 1 T. We observe no evidence of Landau levels or Shubnikov-de Haas oscillations in the non-saturating magnetoresistance, signifying a quenched orbital angular momentum in FeRh.

Tight-binding model. To understand the magnetotransport measurements, we construct a minimal tight-binding model that captures the essential features of the strained thin-film FeRh lattice. We

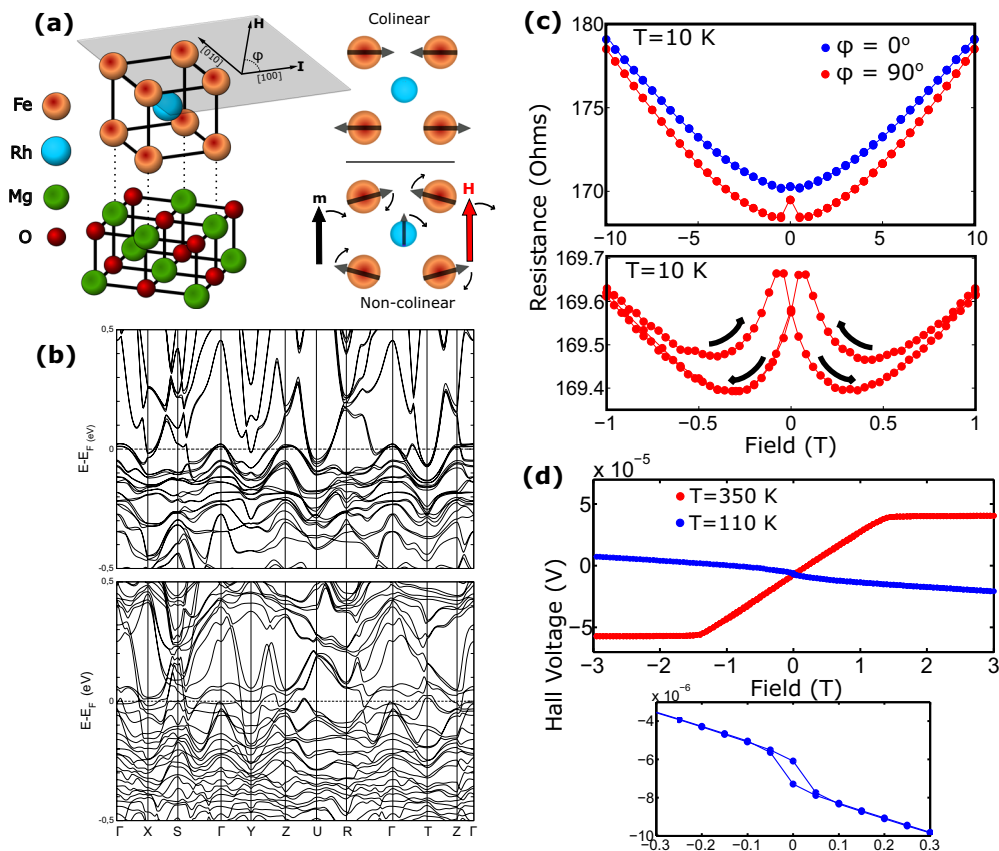


Fig. 1 Characterization and magnetotransport in antiferromagnetic thin-film FeRh. **a** Schematic of the FeRh lattice with epitaxial matching to an MgO substrate. ϕ is the orientation of the external magnetic field, \mathbf{H} , relative to the current along a well-defined crystallographic direction. The behavior of the antiferromagnetic (AFM) order is displayed in the limits of both low and high magnetic fields. An increasing field cants the AFM moments into a non-collinear configuration, and a ferromagnetic moment is generated on the Rh sublattice. The rotation of all magnetization orientations is illustrated as \mathbf{H} rotates. Note that the theoretically expected orthorhombic distortion of the FeRh is not indicated in the schematic. **b** Electronic band structure calculations from density functional theory are shown for the orthorhombic collinear AFM structure (top panel) as well as the non-collinear AFM structure with Rh moment oriented along the [100] direction (bottom panel). **c** The field-dependent magnetoresistance is shown when the field is swept at $\phi = 0^\circ$ and $\phi = 90^\circ$ at $T = 10$ K. The magnetoresistance does not saturate in high-magnetic fields, and the lower plot demonstrates a hysteretic anisotropic magnetoresistance peak at low fields consistent with the presence of residual ferromagnetism. The black arrows denote the direction of the external field sweep. **d** The anomalous Hall effect in both the ferro- and antiferromagnetic phase of FeRh are shown at $T = 350$ K and 110 K respectively. The zero-field anomalous voltage, better seen in the lower plot, indicates the presence of a Berry phase induced by strong spin-orbit coupling the material and is concomitant with the presence of a topological response^{23,24,48,49}.

start with primitive lattice vectors are $a_1 = (100)$, $a_2 = (010)$, and $a_3 = (001)$. Although these lattice vectors are cubic, we allow for terms in the tight-binding model that break the cubic symmetry. To completely capture the orthorhombic structure of the FeRh lattice, the unit cell consists of 8 Fe and 8 Rh atoms. However, to arrive at a qualitatively accurate model of the bands near the Fermi level, we retain only 2 Fe and 2 Rh atoms per unit cell.

The general form of the Hamiltonian is

$$\begin{aligned} H = & \sum_{\langle(i,j)\rangle} t_{ij} c_i^\dagger c_j + \sum_{\langle(i,j)\rangle, (l)} c_i^\dagger i \vec{\lambda}_{ij} \cdot \vec{\sigma} c_j \\ & + \Delta \sum_i \xi c_i^\dagger (\vec{m} \cdot \vec{\sigma}) c_i, \end{aligned} \quad (1)$$

where, $c_i = (c_{i\uparrow}, c_{i\downarrow})^T$ are the electron annihilation operator at site i located at real space point \mathbf{r}_i and $\sigma = (\sigma_x, \sigma_y, \sigma_z)$ represent the Pauli matrices acting on spin, with $\sigma_0 = \mathbb{I}_{2 \times 2}$. The Hamiltonian contains three distinct types of terms: the first sum in Eq. (1) are the spin-independent hopping terms, where $\langle ij \rangle$ indicates the hopping range under consideration and t_{ij} is the corresponding hopping amplitude. The second sum gives the momentum

dependent spin-orbit coupling terms with magnitudes $\vec{\lambda}_{ij}$. In Eq. (1), we have used one s -orbital per atomic site; we justify the approximation as: (1) the Rh atoms are not guaranteed to sit perfectly centered within the Fe atoms in strained FeRh and (2) the orbital structure we utilize provides a sufficient approximation to the projected d -orbital structure in FeRh at half-filling obtained by integrating out the localized orbital moments^{18,19}.

The final term in the Hamiltonian is the AFM exchange term²⁰ that acts on-site and directly competes with the spin-orbit interactions. The AFM interaction is characterized by the magnitude of the exchange, Δ , and the net magnetization orientation, \vec{m} , as illustrated in Fig. 1a. The form of the AFM exchange term is general in nature and is enforced by the presence of the matrix, ξ , that ensures that the sign of the exchange is opposite between successive Fe atoms and zero on the Rh atoms (see Supplementary Note 3, Sec. E3). The AFM exchange term is applicable in the presence of an inhomogeneous interaction, such as the Dzyaloshinskii-Moriya interaction, that may result from the interplay between the spin-orbit interaction and the localized, on-site exchange interactions in FeRh²¹.

To ensure that our reduced FeRh unit cell adequately captures the band crossings at the Fermi level, we constructed an analogous tight-binding model using the full 16 atom unit cell and inspected the band structure as the intracell hopping terms are tuned to arrive at four decoupled 4 atom unit cells. We find that the reduced symmetry of the 4 atom unit cell only affects the energy bands at higher energies than those considered in this work (See Supplementary Note 3 for more details).

We experimentally justify the form of the spin-orbit coupling in Eq. (1) using Fig. 1d, which shows the measured anomalous Hall conductivity (AHC) of the thin-film FeRh devices. The AHC is non-vanishing for both the ferro- and antiferromagnetic phases, demonstrating the presence of strong spin-orbit coupling in FeRh. The anomalous Hall conductivity changes sign in the AFM phase relative to the ferromagnetic phase and, taking into account the residual ferromagnetism at the MgO interface, represents a lower estimate of the anomalous Hall conductivity that is found to be $\sigma_{xy} \approx 10^4 \Omega^{-1} \text{m}^{-1}$. For these measurements the applied magnetic field is out-of-plane in the [001]-direction and the observation of a non-zero AHC in the transport characteristics indicates the presence of Berry curvature in the band structure of FeRh. In other studies of similar non-collinear antiferromagnets, the existence of Berry curvature has been predicted²² and experimentally confirmed^{23,24} via the generation of non-vanishing anomalous Hall voltages. The non-vanishing anomalous voltage at zero-field is attributed to a “remnant” non-collinear configuration that originates from exchange coupling with any remnant residual ferromagnetism on the Rh atoms. Furthermore, recent experiments demonstrate the presence of the inverse spin Hall effect in AFM FeRh, which adds additional support to the presence of strong spin-orbit coupling in this thin-film FeRh²⁵.

FeRh anisotropic magnetoresistance: current in the [100] crystal direction

Experimental results. In Fig. 2a, we show the experimental angular dependence of the AMR for in-plane magnetic fields ranging from 1T to 12T, when the current is along the [100] direction of FeRh. We plot the AMR as $\Delta R/R_{avg}$, where $\Delta R = R(\phi) - R_{avg}$. Here, $R(\phi)$ is the resistance when the magnetic field is at an angle ϕ relative to the [100] current direction, and $R_{avg} = \frac{1}{2\pi} \int_0^{2\pi} R(\phi) d\phi$ is the average resistance over the entire angular range. As previously shown, smooth AMR signals with a continuous derivative with respect to ϕ , arise when the magnetic order parameter continuously rotates with the external magnetic field^{26–29}. Therefore, the continuous AMR we observe in FeRh implies that the $(x-y)$ plane is an easy-plane, consistent with previous experimental studies of FeRh³⁰.

The most striking feature of the AMR is the evolution at fixed ϕ as the magnitude of the in-plane external magnetic field increases. Focusing on $\phi = 0^\circ$ for concreteness, the amplitude of the AMR initially decreases linearly as the magnetic field increases from 1T to 8T, where $\Delta R(\phi = 0) = 0$ at a critical value $B_* \approx 8T$ of the magnetic field. For fields above 8T, the AMR becomes negative and its magnitude increases linearly with increasing magnetic field over the range from 8T to 12T. Similar sign changes in the AMR component have been observed in both ferromagnetic $\text{Co}_x\text{Fe}_{1-x}$ ³¹, as well as in antiferromagnetic materials such as EuTiO_3 ³², and Sr_2IrO_4 ³³. By estimating the magnetic susceptibility of the thin-film geometry, we may map the critical magnetic field at which the sign of the AMR changes, B_* , to a canting angle of $\theta_{cant} \approx 13^\circ$ for the Fe moments. The canting angle, illustrated in Fig. 1a, is calculated assuming a magnetic susceptibility of the thin-film FeRh that is three times greater than previously measured in bulk FeRh³⁴. We note that, due to a

strong diamagnetic background signal from the MgO substrate, direct measurement of the magnetic susceptibility is not possible for the thin-film devices used in this work. We expect the presence of an enhanced susceptibility due to the residual ferromagnetism in the FeRh thin-film, near the MgO interface that provides an additional exchange field that aligns with the external magnetic field.

To quantify the composite amplitudes of each AMR measurement, we perform a spectral analysis of the AMR, writing

$$\Delta R/R_{avg} = \sum_n C_{2n}(B) \cos(2n\phi + \varphi_{2n}). \quad (2)$$

The spectral amplitudes C_{2n} of the experimental AMR are shown in Fig. 2c with corresponding spectral phases φ_{2n} shown in Fig. 2e. We observe that for fields far from B_c the AMR is dominated by the two-fold component C_2 . We also see that $C_2(B_c) = 0$, leading to the dominance of the four-fold harmonic C_4 for fields near B_c .

Theoretical modeling. To understand the AMR results in thin-film FeRh, we next use our 8-band tight-binding model to calculate the AMR for current along the [100] crystal direction at $T = 10$ K. We utilize the tight-binding Hamiltonian in conjunction with the non-equilibrium Green’s function formalism to calculate the observables presented in our work (see Supplementary Note 3 for complete details of the model and Supplementary Table I for the parameter values). As we do not experimentally observe the formation of Landau levels in FeRh, we ignore the orbital effects of the magnetic field. Instead, the external in-plane magnetic field is accounted for by a linear reduction in the antiferromagnetic exchange coupling, Δ and a corresponding linear change in the cant angle of the local moments from $0^\circ - 25^\circ$ ³⁵. As shown in Fig. 2b, we find that the calculated AMR qualitatively captures all of the essential experimentally observed features, including a sign change in $\Delta R(\phi = 0)$, and a transition from two-fold to four-fold to two-fold symmetry as the field passes through a critical value. To facilitate a direct comparison with the experimental data, in Fig. 2d, f, we plot the spectral amplitudes C_{2n} and phases φ_{2n} of the corresponding theoretical data. By comparing Fig. 2c, d, we observe clear qualitative consistencies between theory and experiment. Most notably, we see in the theoretical calculation that the AMR is clearly dominated at all field levels by the twofold symmetric component C_2 for small cant angles until $\theta_{cant} \approx 13.0^\circ$. Furthermore, the sign change of $\Delta R(\phi = 0)$ appears in the spectral decomposition as a change in the phase φ_{2n} by 180° . We observe this at $\theta_{cant}^C = 14.5^\circ$ in Fig. 2e for the theoretical model, and at $\theta_{cant}^E = 13^\circ$ in the experimental data in Fig. 2f.

Moreover, the four-fold symmetric signal (determined by C_4) dominates the observed AMR in FeRh when C_2 component vanishes in both the theoretical and experimental curves. The residual harmonic content, which is small in magnitude both experimentally and theoretically, is dominated by C_4 . The theoretical trend predicts a sign change that is not observed in the experiments at the magnetic fields considered. We attribute this discrepancy to quasiparticle relaxation effects that were not considered in the model, but that naturally occur in the experimental system. Although a full treatment of a disordered quantum transport calculation is beyond the scope of this work, an analysis of random variations of uncorrelated magnetization domains shows that they do not open gaps in the band structure, and hence result in only small changes to the self-energy. While the presence of uncorrelated magnetic domains is insufficient to open a gap in the bands, the overall resistance of the material will increase; however, we expect this effect to average out in $\Delta R/R_{avg}$. Therefore, the quantum transport calculations of the AMR are insensitive to random magnetic disorder³⁶.

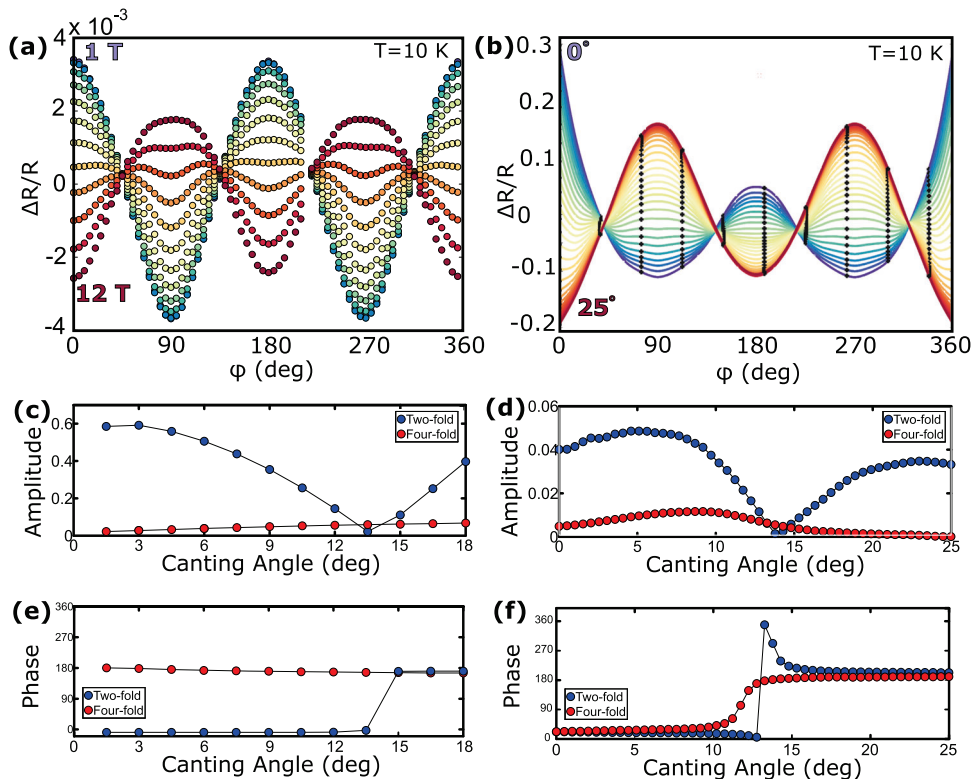


Fig. 2 Quantum transport in the [100] crystal direction. **a** Experimentally measured anisotropic magnetoresistance (AMR) for in-plane magnetic fields between 1-12 T. We see a clear evolution from two-fold (C_2) symmetric AMR at low magnetic fields to a four-fold (C_4), or non-zero coefficient multiplying the $\cos^4\phi$ term in the AMR spectral decomposition, symmetric AMR and returning to an inverted C_2 symmetric AMR at high magnetic fields. **b** Theoretically calculated AMR corresponding to canting angles between the Fe moments that lie in the range of $\theta_{cant} = 0^\circ$ - 25° . The spectral decomposition of **(c)** the experimental and **(d)** the theoretical AMR amplitudes. In **(c)**, we have converted the experimental field to a canting angle by using an assumed magnetic susceptibility for the thin-film samples that is a factor of three greater than the measured bulk magnetic susceptibility of FeRh. The spectral phase of the harmonics, as a function of the canting angle, for both the experimental and theoretical AMR measurements are shown in **(e)** and **(f)**. There is a sharp phase change of 180° in the experimental C_2 harmonic that is accurately captured in the theory at the canting angle where the sign change in the AMR is observed but qualitative differences in the C_4 harmonics exist due to the simplistic nature of the model.

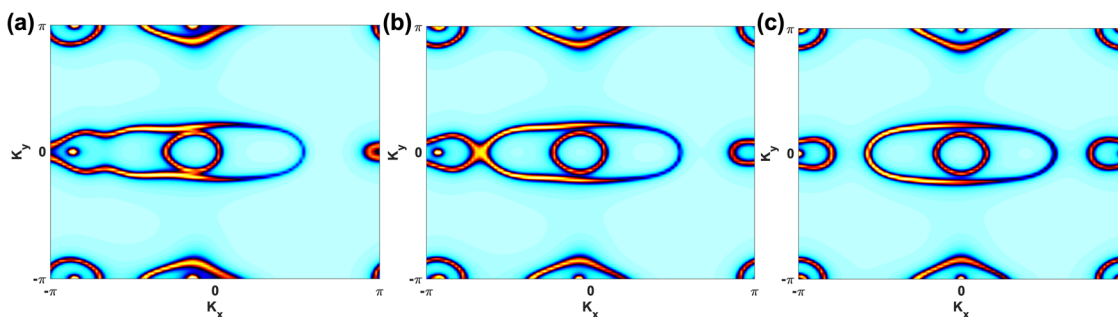


Fig. 3 Spectral density of states in FeRh along the [100]. The spectral density of states (SDOS) when the net magnetization orientation, \hat{m} is pointing orthogonal to the different crystal directions in FeRh under three distinct conditions: (i) $\Delta \gg \lambda$ (ii) $\Delta \approx \lambda$ and (iii) $\Delta \ll \lambda$. The rows of plots represent the three conditions in the crystal grouped according to the net magnetization orientation. In the each horizontal row, we plot the SDOS for each of these conditions respectively from the left to the right for the [100] (a)-(c). The SDOS is plotted in the $k_x - k_y$ -plane at $k_z = 0$. Each of the three cases illustrates a different point in the Lifshitz transition that occurs in FeRh as the in-plane magnetic field is increased. Furthermore, with each successive increase in magnetic field, the pseudogravitational distortion of the Fermi surface geometry increases.

Origin of the AMR: order parameter induced fermi surface deformations. The 8-band model of thin-film FeRh allows us to qualitatively reproduce the observed AMR along the [100] direction. Going further, our model may be utilized to understand the physical origin of the sign change in the AMR, as well as the relative magnitude of C_2 and C_4 as a function of in-plane magnetic field. To do so, we start by examining the local density of states in our tight binding model in three parameter regimes, corresponding to low

($\theta_{cant} < 12^\circ$, $\Delta \gg \lambda$), intermediate ($12^\circ \leq \theta_{cant} \leq 15^\circ$, $\Delta \approx \lambda$) and high cant angles ($\theta_{cant} > 15^\circ$, $\Delta \ll \lambda$). In Fig. 3, we examine each of these three distinct regimes when the magnetic field is oriented perpendicular to the current direction (i.e. $\phi = 90^\circ$) We show the spectral density (SDOS) for the [100] current direction in Fig. 3a when the ($\theta_{cant} = 5^\circ$) there exist clear demarcations of the Fermi surfaces that pass through the constant $E_F = 0eV$ cut at $k_z = 0$ within the $k_x - k_y$ -plane that are connected and reflected about $k_x = k_y = 0$.

Next we increase the cant angle to $\theta_{cant}^{100} = 14^\circ$, as occurs in the experimental measurements via the application of increasing in-plane magnetic fields. In Fig. 3b, we show that this causes the Fermi surfaces to elongate along the [100] direction perpendicular to the [010]-directed external field. By continuing to increase the cant angle in Fig. 3c to be $\theta_{cant}^{100} = 25^\circ$, corresponding to the point when $C_2 = 0$. In each case the formerly concentric Fermi surfaces become disconnected. Crucially, we note that the Fermi contours touch at the same point in parameter space where $C_2 = 0$. The Lifshitz transition in the Fermi surface geometry is thus correlated with the sign change in the AMR. Finally, as the cant angle continues to increase under concomitant increases in the external magnetic field, the Fermi surfaces illustrated in the SDOS of Fig. 3, become distorted in the direction perpendicular to the external magnetic field, resulting in the observed AMR where $C_2 < 0$.

Using the 8-band model for FeRh, we observe that there is a correlation between the change in the sign of C_2 and a change in geometry and topology of the Fermi surface that occurs as the cant angle is increased. The appearance of a Lifshitz transition as the cant angle, or the ratio of exchange energy to spin-orbit interaction, changes is indicative of a deep connection between the geometry of the Fermi surface and the magnetic order parameter that manifest in the change in sign of the AMR. To clarify the underlying physics, we now construct a minimal model that contains the crucial physical attributes associated with the Lifshitz transition, spin-orbit coupling and the magnetic exchange interaction. To this end, we examine a 2-band ferromagnetic Rashba spin-orbit coupled metal in two dimensions. The Hamiltonian for the the ferromagnetic metal is

$$H_{EM} = \sum_{\sigma, (ij)} -tc_{i\sigma}^\dagger c_{j\sigma} + i\lambda_R c_{i\sigma}^\dagger \hat{z} \times \vec{\sigma}^{\sigma\sigma'} c_{j\sigma'} + \sum_i c_{i\sigma}^\dagger \vec{\Delta} \cdot \vec{\sigma}^{\sigma\sigma'} c_{j\sigma'} + \sum_{\sigma, i} (4t - \mu) c_{i\sigma}^\dagger c_{i\sigma}, \quad (3)$$

where t is the nearest-neighbor hopping amplitude, λ_R is the Rashba spin-orbit coupling strength, $\vec{\Delta}$ is the ferromagnetic order parameter that may be manipulated in the same manner as Eq. (1), and μ is the chemical potential. Note, however, that unlike in FeRh, here the value of $|\Delta|$ increases with the external magnetic field due to the ferromagnetic nature of the pairing. In the context of the model, we note that σ need not represent the physical spin degree of freedom, instead it may be a spin-orbit coupled degree of freedom that is projected into a set of low-energy bands, as in an antiferromagnet. In Fig. 4a, we utilize the ferromagnetic Rashba model to calculate the AMR as we rotate the magnetic order parameter. This allows us to emulate the physics of FeRh in the three critical regions surrounding the sign change of C_2 , and thus to codify the interaction between magnetism, Fermi surface geometry, and the spin-orbit interaction. We observe that the three AMR curves faithfully reproduce the intricate physics observed in the more complex tight-binding model for FeRh.

First, we consider the limit $\Delta \gg \lambda_R$, where the chemical potential, μ , cuts across only one of the two spin-split bands. This results in a spin non-degenerate Fermi surface, as shown in Fig. 4b. In exploring the Fermi surface, we position the magnetic order parameter along the \hat{y} -direction and find the same distortion of the Fermi surface perpendicular to the direction of the order parameter as in our model of FeRh. The result of having a single non-degenerate Fermi surface at the Fermi energy is a two-fold symmetric AMR with a maximum at $\phi = 0^\circ$, or $C_2 > 0$. Next, when $\Delta \sim \lambda_R$, we observe a Lifshitz transition, in Fig. 4c. As in FeRh, the AMR corresponding to the onset of the Lifshitz transition contains multiple harmonics of comparable magnitude.

Beyond the Lifshitz transition ($\Delta \ll \lambda_R$), the ferromagnetic Rashba model has two concentric Fermi surfaces when $|\vec{\Delta}| \rightarrow 0$, which become distorted for non-zero $|\Delta|$, as seen in Fig. 4d (See Supplementary Note 3 for more details).

Nevertheless, it is clear that the change in the resistance of the 2-band ferromagnetic Rashba model, computed as a function of order parameter strength and orientation, captures the essential features of the more complicated 8-band model of FeRh. In particular, for small $|\vec{\Delta}|$ the AMR is predominantly two-fold symmetric, with a minimum of the resistance at $\phi = 0$ ($C_2 < 0$) as in the extreme spin-orbit coupled limit of FeRh.

AMR from pseudogravitational fields. Both the more accurate 8-band model of FeRh and the more simplified 2 band model of the ferromagnetic Rashba metal point to the onset of a sign change in the AMR as a ubiquitous feature present in the AMR of spin-orbit coupled magnetic materials. Beginning with this observation, we propose a geometric framework within which to understand these effects that is rooted in the observation that the distortions of the Fermi surface in both the FeRh and ferromagnetic Rashba model bear a striking resemblance to the coupling of fermions to curved space. For a quadratically dispersing band, as in the ferromagnetic Rashba model with a small Fermi surface, the Fermi surface distortion may be parametrized by an effective low-energy Hamiltonian as

$$H_{eff}^{quad} = g^{ij}(\Delta) k_i k_j, \quad (4)$$

where the effective nonrelativistic “metric” tensor $g^{ij}(\Delta)$ is a function of the magnetic order parameter and its form determines the observed Fermi surface geometry. The geometric coupling arises due to the non-trivial SOC-induced winding of the spin texture on the Fermi surface interacting with the background magnetic order parameter, and therefore, is intimately connected band topology. For the Rashba model with a constant background magnetic order parameter, the metric describes an elliptical distortion of the Fermi surface; for larger Fermi surfaces, where quartic corrections to the dispersion become important, we recover Fermi surface geometries such as in Fig. 4.

Due to the gravitational parallel we have exploited in our Fermi surface parametrization, where the coupling of the order parameter to the carriers results in a distorted Fermi surface, we refer to the coupling of the order parameter to the Fermi surface geometry as “pseudogravity”. As we will see via the example of the Rashba model below, pseudogravitational fields are expected to arise whenever there is magnetic order in the presence of spin-orbit coupling. For systems such as FeRh which feature linearly-dispersing Weyl fermions in addition to quadratically dispersing Fermi pockets, we expect the Weyl fermions to be coupled to a relativistic pseudogravitational metric of the form^{37,38}

$$g^{\mu\nu} = e^\mu{}_\alpha e^\nu{}_\beta \eta_{\alpha\beta} = \left(\begin{array}{c|c} -1 & -\mathbf{u} \\ \hline -\mathbf{u} & AA^T \end{array} \right). \quad (5)$$

In Eq. (5), we show the metric in block matrix form expressed with the Minkowski signature typical of flat spacetime. The off-diagonal components of Eq. (5), \mathbf{u} may be interpreted as the velocity of a moving frame, or a tilt in the case of a Weyl semimetal^{37,39}, and A parametrizes the elliptical distortion of the Fermi surface.

Using the Rashba model as a simple example, we will now see how anisotropic magnetoresistance is a signature of pseudogravitational couplings. For a noninteracting system with nonmagnetic disorder, contributions to the ohmic conductivity originate from

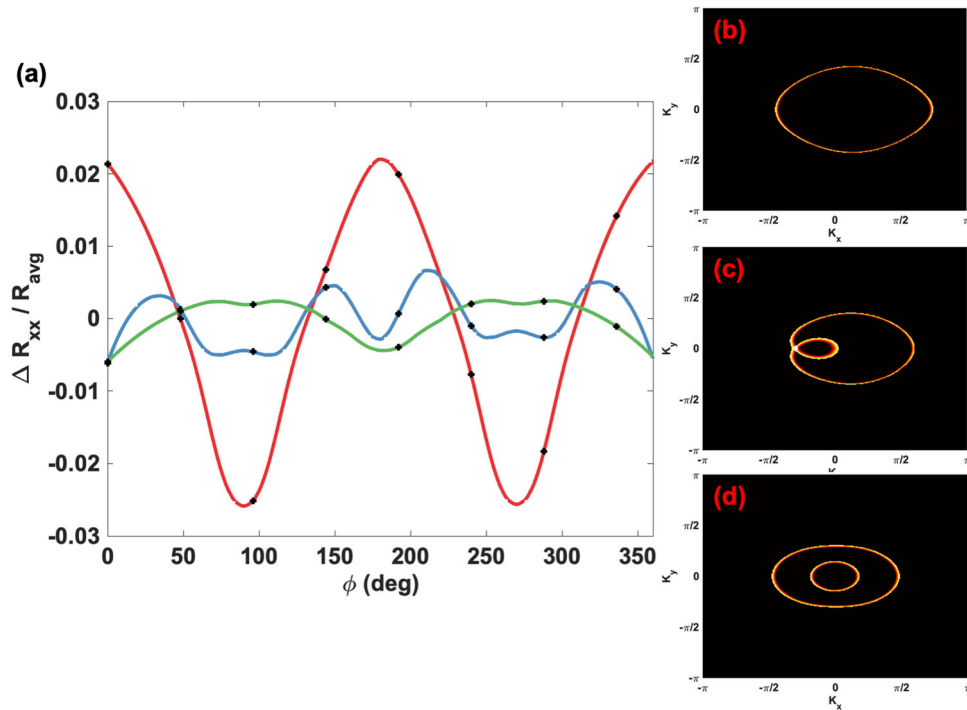


Fig. 4 Quantum transport in a Rashba spin-orbit coupled ferromagnet. **a** Numerically calculated anisotropic magnetoresistance (AMR) corresponding to a spin orbit coupling of $\lambda_R = 0.5$, a chemical potential of $\mu = 0.2$, and $\Delta = 0.9$ (red), $\Delta = 0.5$ (blue) and $\Delta = 0.01$ (green) where in each case the magnetic order parameter is oriented along the \hat{y} -direction in the model. **b** The distorted non-degenerate Fermi surface corresponding to the C_2 symmetric AMR of $\Delta = 0.9$ **c** The Fermi surface when $\Delta = 0.5$ shows the appearance of a second concentric Fermi surface at the Fermi level that is indicative of the onset of a Lifshitz transition resulting in the appearance of harmonics beyond that of C_2 . **d** The Fermi surface corresponding to $\Delta = 0.01$ where the Fermi level crosses both spin bands resulting in concentric spin-degenerate Fermi surfaces and the recovery of an inverted C_2 -symmetric AMR, as seen in FeRh.

electrons near the Fermi surfaces, which, as in Fig. 4, distort as a function of $|\vec{\Delta}|$ and ϕ . In particular, within the relaxation time approximation and with nonmagnetic disorder the dissipative conductivity depends on the geometry of bands near the Fermi surface, and is given by the Fermi surface integral

$$\sigma_{ij} \propto \int d^2k \left(\frac{\partial \epsilon_{\mathbf{k}}}{\partial k_i} \frac{\partial \epsilon_{\mathbf{k}}}{\partial k_j} \right) \delta(\mu - \epsilon_{\mathbf{k}}). \tag{6}$$

around the Fermi surface with energy $\epsilon_{\mathbf{k}}$. We separate our analysis in the two regimes in the AMR that are of interest: $\Delta \gg \lambda_R$, where the C_2 harmonics dominate, and $\Delta \ll \lambda_R$, where similar C_2 harmonics dominate but with a $\frac{\pi}{2}$ phase shift.

We begin by examining the limit $\Delta \gg \lambda$ where we seek both an expression for the effective metric and the conductivity. In this limit, we further restrict ourselves to negative values of the chemical potential μ , such that we have a single Fermi surface.

In this limit, we may write the Bloch Hamiltonian corresponding to Eq. (3) as

$$H(\mathbf{k}) = \sigma_0 [2t(2 - \cos k_x - \cos k_y) - \mu] + \Delta \cdot \vec{\sigma} + \lambda_R (\sin k_x \sigma_y - \sin k_y \sigma_x) \tag{7}$$

Since, we have chosen μ such that the Fermi surface is small, we may expand the Hamiltonian about $\mathbf{k} = 0$ to find

$$H(\mathbf{k}) \approx [t(k_x^2 + k_y^2) - \mu] \sigma_0 + \Delta \cdot \vec{\sigma} + \lambda_R (k_x \sigma_y - k_y \sigma_x) \tag{8}$$

with corresponding energies

$$E_{\pm} = t|k|^2 - \mu \pm \sqrt{(\lambda_R k_x + \Delta \sin \phi)^2 + (\lambda_R k_y - \Delta \cos \phi)^2} \tag{9}$$

Let us now suppose that when $\Delta \gg \lambda_R$, the Fermi surface lies entirely in the E_- band. By expanding occupied band, E_- , in

powers of λ_R/Δ to find the effective Hamiltonian that is quadratic in momentum, as expected from Eq. (4), or

$$E_- \approx \Delta + t|k|^2 - \mu + \lambda_R (k_x \sin \phi - k_y \cos \phi) + \frac{\lambda_R^2}{2\Delta} (k_x \cos \phi + k_y \sin \phi)^2. \tag{10}$$

We see that, to lowest order the energy, E_- is a quadratic form in momentum, \mathbf{k} , and we may complete the square to write,

$$E_- = E_{-0} + g_{ij}(\phi) k'_i k'_j, \tag{11}$$

where to lowest order we may make the following substitutions in Eq. (10) to arrive at the Eq. (11)

$$k'_x = k_x + \lambda_R \sin \phi / 2t \tag{12}$$

$$k'_y = k_y - \lambda_R \cos \phi / 2t \tag{13}$$

$$E_{-0} = \Delta - \mu + \lambda_R^2 (\sin \phi - \cos \phi)_{ij} g_{ij} \begin{pmatrix} \sin \phi \\ -\cos \phi \end{pmatrix} \tag{14}$$

$$g_{ij} = \begin{pmatrix} t + \frac{\lambda_R^2}{2\Delta} \cos^2 \phi & \sin \phi \cos \phi \frac{\lambda_R^2}{2\Delta} \\ \sin \phi \cos \phi \frac{\lambda_R^2}{2\Delta} & t + \frac{\lambda_R^2}{2\Delta} \sin^2 \phi \end{pmatrix}_{ij}. \tag{15}$$

Eq. (15) gives the pseudogravitational metric $g_{ij}(\phi)$ as a function of the tight-binding parameters. The metric $g_{ij}(\phi)$ naturally emerges from the parametrization after the low-momentum expansion. The presence of the pseudogravitational metric is expected here as it determines the geometry of the Fermi surface which, in turn, sets the velocity at the Fermi surface. Substituting Eq. (11) this into Eq. (6) for the conductivity, we find that

$$\sigma_{ij}(\phi) = \frac{1}{\sqrt{\det g_{ij}(|\Delta|, \phi)}} g_{ij}(|\Delta|, \phi) \bar{\sigma}_0. \quad (16)$$

where $\bar{\sigma}_0$ is a ϕ -independent but μ and t -dependent constant. Eq. (16) shows that the conductivity tensor in this limit is a function of the pseudogravitational metric. To find the AMR, we invert Eq. (16) resulting in an equation for the longitudinal resistivity as a function of ϕ , $\frac{Q\mathcal{E}}{\lambda_R^2}$

$$\rho_{xx}(\phi) = \bar{\rho} + \frac{Q\mathcal{E}}{4t\Delta} \cos 2\phi + \mathcal{O}(\lambda_R^3). \quad (17)$$

Eq. (17) reproduces the positive two-fold dominant, C_2 , AMR observed in the high-field magnetic field limit of both the 8-band tight-binding model for FeRh and the 2-band Rashba model. In our analysis, we note that including the next-order correction to Eq. (17) produces a term that is proportional to $\cos 4\phi$. The C_4 dominant Fourier harmonic is observed both experimentally and numerically when $\Delta \approx \lambda_R$ when the Fermi surface is close to the onset of the Lifshitz transition.

Next, we examine the conductivity in the low magnetic field limit, or when $\Delta \ll \lambda_R$. In this limit, we expand the energies E_{\pm} in Eq. (9) in powers of $\Delta/\lambda_R \ll 1$. We take advantage of the fact that the spin-orbit coupling, λ_R , multiplies the momentum, $|\vec{k}|$, in Eq. (9) to make a change of variables such that

$$\vec{k}' = \vec{k} + \frac{\Delta}{\lambda_R} (\sin \phi, -\cos \phi). \quad (18)$$

In terms of adjusted momentum, \vec{k}' , we may rewrite the energies for the 2-band Hamiltonian of Eq. (9) in the low-field limit as

$$E_{\pm} = t|\vec{k}'|^2 \pm \lambda_R |\vec{k}'| \left(1 \mp \frac{2t\Delta}{\lambda_R^2} \sin(\phi - \theta) \right) + \frac{t\Delta^2}{\lambda_R^2} - \mu \quad (19)$$

We see that, distinct from the $\Delta \gg \lambda_R$ limit, in the $\Delta \ll \lambda_R$ limit the constant E_{\pm} contours are anisotropic and depend explicitly on the angle $\theta - \phi$ between \vec{k}' and $\vec{\Delta}$. This dependence, combined with the explicit dependence of the energy on $|\vec{k}'|$ indicates that the constant energy surfaces of Eq. (19) do not admit a description in terms of a quadratic form; in this limit, the Fermi surfaces of the Rashba model are quartic surfaces. Nevertheless, we observe that by rotating the order parameter, or changing ϕ induces a distortion of the constant energy contours of Eq. (19).

In a similar fashion to the high-field limit, we may use Eq. (6) to evaluate the conductivity of the Rashba model perturbatively in Δ/λ_R . In the low-field limit, however, we find that the anisotropy in the conductivity tensor arises due to the $\vec{\Delta}$ dependence of the quartic Fermi surface shape and, by extension, the Fermi velocity. The presence of the quartic Fermi surface in this limit does not admit a simple analytic solution, as was the case in the high-field limit. On the other hand, in the limit that the chemical potential, μ lies in between the upper and lower spin-split bands, ensuring that there is only a single large Fermi surface, we may numerically solve for the conductivity and resistivity to find that the AMR for the Rashba model is C_2 dominant and negative in the $\Delta \ll \lambda_R$ limit.

We may now understand the core physical rationale behind the appearance of the Lifshitz transition in the FeRh and ferromagnetic Rashba AMR. In both the $\Delta \ll \lambda_R$ and $\Delta \gg \lambda_R$ limits, we have a strong interdependence between the magnetic order parameter and the spin-orbit coupling. Therefore, under the application of a strong in-plane magnetic field, the pseudogravitational fields couple to the electrons on the Fermi surface leading to the distortions, seen in Figs. 3 and 4. Continued increases in magnetic field leads to increasing pseudogravitational

modification of the Fermi surface that pulls the connected Fermi pockets apart leading to the observed features in the AMR. As we see in Eq. (16), when the Fermi surface is approximately quadratic, the pseudogravitational distortion directly determines the conductivity tensor and hence the AMR.

The end result is that we arrive at a simple interpretation of the observed AMR: the interplay between spin-orbit coupling and magnetic order creates a pseudogravitational coupling between the order parameter, the Fermi surface shape that alters the resultant quasiparticle velocity. The AMR in our 8-band model of FeRh arises from a similar mechanism and, although the coupling between the order parameter and the 4 bands crossing the Fermi surface is more intricate in FeRh, we nevertheless observe in Fig. 4 that the AFM order parameter distorts the Fermi surfaces leading to the observed AMR. We note that our calculations for both the Rashba and 8-band FeRh model treat disorder as non-magnetic in nature within the relaxation time approximation. However, since the corresponding self-energies from relevant phonon or spin-fluctuation contributions are small in magnitude, their presence would not impact the results presented in this work⁴⁰.

Conclusions

In this work, we have measured the anisotropic magnetoresistance of thin-film FeRh samples in the antiferromagnetic regime. We showed that as the magnetic field rotates, the order parameter smoothly tracks the magnetic field direction. Through a combination of ab-initio calculations and tight-binding modeling of thin-film FeRh, we showed how the observed AMR is a result of the evolution of the Fermi surface geometry as a function of applied magnetic field. We demonstrated that the coupling between the inherent magnetic order and Fermi surface geometry is ubiquitous in spin-orbit coupled magnets and is responsible for the most salient observables in the AMR measurements. Using a simplified ferromagnetic Rashba model, we are able to illustrate the origin of this coupling: spin-orbit coupling induces Fermi-surface spin textures that are influenced by the magnetic order. With the aid of a $\mathbf{k} \cdot \mathbf{p}$ approximation for small Fermi surfaces in the Rashba model, we find that the distortion of the Fermi surface plays the role of an anisotropic band mass tensor that depends on the magnetic order parameter. From a theoretical perspective, this tunable band mass anisotropy is analogous to an effective pseudogravitational metric,

$$\frac{1}{2m} \sum_i k_i^2 \rightarrow \sum_{ij} g^{ij}(|\Delta|, \phi) k_i k_j, \quad (20)$$

that allowed for a much deeper understanding of the underlying physics associated with the Lifshitz transition. In FeRh, we have linearly dispersing Weyl pockets near the Fermi level in addition to typical quadratic metallic Fermi surfaces. As such, we expect these Weyl Fermi surfaces are also similarly distorted due to the coupling between spin-orbit interaction and magnetism. Using the analysis associated with the pseudogravitational mapping will shed light on observations in other magnetic systems that possess both topological and mean-field order such as EuTiO_3 ³². In a broader context, our results suggest that easy-plane antiferromagnets with strong spin-orbit coupling are candidate systems for exploring the coupling of fermions to distorted background geometries.

Methods

FeRh crystal growth. The FeRh films used in this work have been deposited onto [001]-oriented MgO substrates using DC magnetron sputtering. Prior to sputtering, the substrates are heated within the sputter deposition system to 850 °C for 1 h to ensure

that potential contaminants are desorbed from the surface. After the substrates are cleaned, the temperature was lowered to 450 °C for deposition. The sputter target used for deposition is an equiatomic FeRh source. During growth, 6.5 sccm of Ar gas was introduced into the chamber, and the pressure was set to 6 mTorr. The DC sputtering power used was 50 W, and the growth rate was 0.7 Å/s.

FeRh device fabrication. A photolithographically patterned mask has been developed onto a continuous film in the intended Hall bar pattern, and an ion-milling process removes the FeRh film not under the mask. Magnetotransport measurements were made inside a Quantum Design, Physical Properties Measurement System (PPMS). Longitudinal magnetoresistance and transverse voltage measurements of samples were made using standard lock in detection with a Stanford Research Systems SR830 lock in amplifier. To facilitate lock-in detection, a 17 Hz probe current of nominally 10 μ A was used.

Density functional calculations of FeRh. To perform DFT calculations, we use the Vienna Ab-Initio Simulation Package^{41,42} (VASP). The projected augmented wave (PAW) pseudopotentials⁴³ are used for the calculations and the exchange-correlation energy is calculated with generalized gradient approximation (GGA) in the Perdew-Burke-Ernzerof form⁴⁴. A Γ -centered $11 \times 11 \times 11$ Monkhorst-Pack k -mesh is used for the calculations. We reproduce the Dzyaloshinskii-Moriya interaction (DMI) using the constrained moment approach with spin-orbit coupling interactions implemented in VASP so as to calculate the band structure for different spin orientations^{45–47}. In order to reproduce the strong correlation of the d -orbitals that drives the magnetism, we use a Hubbard U of 3 eV for both magnetic atoms. In order to understand the evolution of the bandstructure under the experimental conditions presented in the main text, we must be able to approximate the effects of an in-plane magnetic field on the thin-film FeRh. In our work, we mimic the magnetic field by configuring the normally non-magnetic Rh magnetic moments to be configured in such a manner so as to possess an in-plane ferromagnetic orientation. One of the important consequences of the Rh atoms developing an in-plane ferromagnetic state is that the nature of the FeRh crystal changes from symmorphic to non-symmorphic.

Data availability

The data that support the findings of this study are available from the corresponding author upon reasonable request.

Received: 5 September 2022; Accepted: 2 August 2023;

Published online: 06 September 2023

References

- Hasan, M. Z. & Kane, C. L. Colloquium: topological insulators. *Rev. Mod. Phys.* **82**, 3045 (2010).
- Qi, X.-L. & Zhang, S.-C. Topological insulators and superconductors. *Rev. Mod. Phys.* **83**, 1057 (2011).
- Sato, M. & Ando, Y. Topological superconductors: a review. *Rep. Prog. Phys.* **80**, 076501 (2017).
- Xu, S.-Y. et al. Discovery of a weyl fermion semimetal and topological fermi arcs. *Science* **349**, 613–617 (2015).
- Yan, B. & Felser, C. Topological materials: Weyl semimetals. *Annu. Rev. Condens. Matter Phys.* **8**, 337–354 (2017).
- Armitage, N., Mele, E. & Vishwanath, A. Weyl and dirac semimetals in three-dimensional solids. *Rev. Mod. Phys.* **90**, 015001 (2018).
- Fang, C., Gilbert, M. J. & Bernevig, B. A. Topological insulators with commensurate antiferromagnetism. *Phys. Rev. B* **88**, 085406 (2013).
- Šmejkal, L., Mokrousov, Y., Yan, B. & MacDonald, A. H. Topological antiferromagnetic spintronics. *Nat. Phys.* **14**, 242 (2018).
- Smejkal, L., Mokrousov, Y., Yan, B. & MacDonald, A. H. Topological antiferromagnetic spintronics. *Nat. Phys.* **14**, 242–251 (2018).
- Niu, C. et al. Antiferromagnetic topological insulator with nonsymmorphic protection in two dimensions. *Phys. Rev. Lett.* **124**, 066401 (2020).
- Bonbien, V. et al. Topological aspects of antiferromagnets. *J. Phys. D: Appl. Phys.* **55**, 103002 (2021).
- Saglam, H. *Spin Transport and Spin-Orbit Torques in Antiferromagnets* (Illinois Institute of Technology, 2019).
- Fan, R. et al. Ferromagnetism at the interfaces of antiferromagnetic ferh epilayers. *Phys. Rev. B* **82**, 184418 (2010).
- Zarkevich, N. A. & Johnson, D. D. Ferh ground state and martensitic transformation. *Phys. Rev. B* **97**, 014202 (2018).
- Lewis, L., Marrows, C. & Langridge, S. Coupled magnetic, structural, and electronic phase transitions in ferh. *J. Phys. D: Appl. Phys.* **49**, 323002 (2016).
- Han, G. et al. Suppression of low-temperature ferromagnetic phase in ultrathin ferh films. *J. Appl. Phys.* **113**, 123909 (2013).
- Jaccard, Y., Guittienne, P., Kelly, D., Wegrowe, J.-E. & Ansermet, J.-P. Uniform magnetization rotation in single ferromagnetic nanowires. *Phys. Rev. B* **62**, 1141 (2000).
- Khan, M., Khwaja, Y. & Demangeat, C. Origin of giant moments in non-stoichiometric ferh alloys. *J. Phys.* **42**, 573–577 (1981).
- Hasegawa, H. Electronic structures and local magnetic moments in ferromagnetic and antiferromagnetic fe_xrh_{1-x} alloys. *J. Magn. Magn. Mater.* **66**, 175–186 (1987).
- Tang, P., Zhou, Q., Xu, G. & Zhang, S. C. Dirac fermions in an antiferromagnetic semimetal. *Nat. Phys.* **12**, 1100 (2016).
- Bogdanov, A. N., Röfler, U. K., Wolf, M. & Müller, K. H. Magnetic structures and reorientation transitions in noncentrosymmetric uniaxial antiferromagnets. *Phys. Rev. B* **66**, 214410 (2002).
- Chen, H., Niu, Q. & MacDonald, A. H. Anomalous hall effect arising from noncollinear antiferromagnetism. *Phys. Rev. Lett.* **112**, 017205 (2014).
- Nakatsuji, S., Kiyohara, N. & Higo, T. Large anomalous hall effect in a noncollinear antiferromagnet at room temperature. *Nature* **527**, 212–215 (2015).
- Nayak, A. K. et al. Large anomalous hall effect driven by a nonvanishing berry curvature in the nonlinear antiferromagnet mn_3ge . *Sci. Adv.* **2**, e1501870 (2016).
- Wang, Y. et al. Spin pumping during the antiferromagnetic–ferromagnetic phase transition of iron–rhodium. *Nat. Commun.* **11**, 1–8 (2020).
- Oh, J., Humbard, L., Humbert, V., Sklenar, J. & Mason, N. Angular evolution of thickness-related unidirectional magnetoresistance in co/pt multilayers. *AIP Adv.* **9**, 045016 (2019).
- Baldreti, L. et al. Full angular dependence of the spin hall and ordinary magnetoresistance in epitaxial antiferromagnetic nio (001)/pt thin films. *Phys. Rev. B* **98**, 024422 (2018).
- Cheng, Y. et al. Anisotropic magnetoresistance and nontrivial spin hall magnetoresistance in pt/ α -fe₂o₃ bilayers. *Phys. Rev. B* **100**, 220408 (2019).
- Fischer, J. et al. Large spin hall magnetoresistance in antiferromagnetic α -fe₂o₃/pt heterostructures. *Phys. Rev. Appl.* **13**, 014019 (2020).
- Marti, X. et al. Room-temperature antiferromagnetic memory resistor. *Nat. Mater.* **13**, 367 (2014).
- Zeng, F. L. et al. Intrinsic mechanism for anisotropic magnetoresistance and experimental confirmation in co_xfe_{1-x} single-crystal films. *Phys. Rev. Lett.* **125**, 097201 (2020).
- Ahadi, K. et al. Anisotropic magnetoresistance in the itinerant antiferromagnetic $eutio_3$. *Phys. Rev. B* **99**, 041106 (2019).
- Wang, C. et al. Anisotropic magnetoresistance in antiferromagnetic sr₂iro₄. *Phys. Rev. X* **4**, 041034 (2014).
- Navarro, E., Hernando, A., Yavari, A., Fiorani, D. & Rosenberg, M. Grain-boundary magnetic properties of ball-milled nanocrystalline fe_xrh_{100-x} alloys. *J. Appl. Phys.* **86**, 2166–2172 (1999).
- Takahashi, M. & Tsunoda, M. Magnetic anisotropy of antiferromagnet and its role on the exchange bias in ferromagnetic/antiferromagnetic bilayers. *J. Phys. D: Appl. Phys.* **35**, 2365 (2002).
- Kim, Y., Kang, K., Schleife, A. & Gilbert, M. J. Voltage-induced switching of an antiferromagnetically ordered topological dirac semimetal. *Phys. Rev. B* **97**, 134415 (2018).
- Nissinen, J. & Volovik, G. Elasticity tetrads, mixed axial-gravitational anomalies, and (3+1)-d quantum hall effect. *Phys. Rev. Res.* **1**, 023007 (2019).
- Landsteiner, K., Megias, E. & Pena-Benitez, F. Gravitational anomaly and transport phenomena. *Phys. Rev. Lett.* **107**, 021601 (2011).
- Bradlyn, B. & Read, N. Low-energy effective theory in the bulk for transport in a topological phase. *Phys. Rev. B* **91**, 125303 (2015).
- Kim, Y., Park, M. J., Cahill, D. G. & Gilbert, M. J. Impact of thermal fluctuations on transport in antiferromagnetic semimetals. *Phys. Rev. B* **98**, 024409 (2018).
- Kresse, G. & Furthmüller, J. Efficiency of ab-initio total energy calculations for metals and semiconductors using a plane-wave basis set. *Comput. Mater. Sci.* **6**, 15–50 (1996).

42. Kresse, G. & Hafner, J. Ab initio molecular dynamics for open-shell transition metals. *Phys. Rev. B* **48**, 13115–13118 (1993).
43. Kresse, G. & Joubert, D. From ultrasoft pseudopotentials to the projector augmented-wave method. *Phys. Rev. B* **59**, 1758–1775 (1999).
44. Perdew, J. P., Burke, K. & Ernzerhof, M. Generalized gradient approximation made simple. *Phys. Rev. Lett.* **77**, 3865–3868 (1996).
45. Yang, H., Thiaville, A., Rohart, S., Fert, A. & Chshiev, M. Anatomy of dzyaloshinskii-moriya interaction at Co/Pt interfaces. *Phys. Rev. Lett.* **115**, 267210 (2015).
46. Xiang, H. J., Kan, E. J., Wei, S.-H., Whangbo, M.-H. & Gong, X. G. Predicting the spin-lattice order of frustrated systems from first principles. *Phys. Rev. B* **84**, 224429 (2011).
47. Lu, X. Z., Whangbo, M.-H., Dong, S., Gong, X. G. & Xiang, H. J. Giant ferroelectric polarization of $\text{CaMn}_7\text{O}_{12}$ induced by a combined effect of dzyaloshinskii-moriya interaction and exchange striction. *Phys. Rev. Lett.* **108**, 187204 (2012).
48. Huang, X. et al. Observation of the chiral-anomaly-induced negative magnetoresistance in 3d weyl semimetal taas. *Phys. Rev. X* **5**, 031023 (2015).
49. Liu, E. et al. Giant anomalous hall effect in a ferromagnetic kagome-lattice semimetal. *Nat. Phys.* **14**, 1125–1131 (2018).

Acknowledgements

This research was primarily supported by the NSF through the University of Illinois at Urbana-Champaign Materials Research Science and Engineering Center DMR-1720633. Thin-film growth at Argonne National Laboratory was supported by the U.S. Department of Energy, Office of Science, Materials Science and Engineering Division. B.B. acknowledges the support of the Alfred P. Sloan foundation, and the National Science Foundation under grant DMR-1945058. M.G.V. and J.O. acknowledge support from ONR 14-17-1-3012. M.G.V. thanks support from the Spanish Ministry of Science and Innovation (grant number PID2019-109905GB-C21) and thanks F. Orlandi for discussions.

Author contributions

J.S. and N.M. designed the magnetotransport experiments. H.S. and A.H. were responsible for synthesizing FeRh films. J.S., S.S., and H.S. performed magnetic and structural characterization of FeRh. J.S., J.O., and H.S. fabricated devices. J.S., S.S., and J.O. performed magnetotransport experiments. A.H. and N.M. supervised the

experimental work. M.V. performed DFT calculations with input from M.G. and B.B. on magnetic structure. M.G.V. and B.B. developed the theoretical models and quantum transport simulations. M.G.V. and B.B. analyzed the results with J.S., A.H. and N.M. providing input. B.B. and M.G.V. wrote the manuscript with input from all other authors.

Competing interests

The authors declare no competing interests.

Additional information

Supplementary information The online version contains supplementary material available at <https://doi.org/10.1038/s42005-023-01335-5>.

Correspondence and requests for materials should be addressed to Matthew J. Gilbert.

Peer review information *Communications Physics* thanks Antonio Gallerati, and the other, anonymous, reviewer(s) for their contribution to the peer review of this work.

Reprints and permission information is available at <http://www.nature.com/reprints>

Publisher's note Springer Nature remains neutral with regard to jurisdictional claims in published maps and institutional affiliations.



Open Access This article is licensed under a Creative Commons Attribution 4.0 International License, which permits use, sharing, adaptation, distribution and reproduction in any medium or format, as long as you give appropriate credit to the original author(s) and the source, provide a link to the Creative Commons licence, and indicate if changes were made. The images or other third party material in this article are included in the article's Creative Commons licence, unless indicated otherwise in a credit line to the material. If material is not included in the article's Creative Commons licence and your intended use is not permitted by statutory regulation or exceeds the permitted use, you will need to obtain permission directly from the copyright holder. To view a copy of this licence, visit <http://creativecommons.org/licenses/by/4.0/>.

© The Author(s) 2023